CCFE
CULHAM CENTRE FOR FUSION ENERGY

UK Atomic Energy Authority

UKAEA-CCFE-PR(24)236

M. Pacella, S. Silburn, P. Ghosh, S. Chen, G. Matthews

Laser Surface Engineering of Inconel 625 tiles to manufacture high thermal emitters

Laser Surface Engineering of Inconel 625 tiles to manufacture high thermal emitters

M. Pacella, S. Silburn, P. Ghosh, S. Chen, G. Matthews

This is a preprint of a paper submitted for publication in
Surface and Coatings Technology

Laser Surface Engineering of Inconel 625 tiles to manufacture high thermal emitters

Manuela Pacella[a,*], Scott Silburn[b], Priyanka Ghosh[a], Sunchi Chen[b], Guy Matthews[b]

[a] Wolfson School of Mechanical, Electrical and Manufacturing Engineering, Loughborough University, Loughborough, Leicestershire, LE11 3TU, UK

[b] United Kingdom Atomic Energy Authority, Culham Campus, Abingdon, Oxon, OX14 3DB, UK

Abstract

Inconel 625 is a nickel-chromium based super alloy used in the construction of the vacuum vessel of the Joint European Torus (JET) experimental fusion device. It was selected for its mechanical properties at elevated temperature, being exposed to vacuum baking at >300°C and heat loads of typically 0.5 MW/m^2 for recessed areas of the JET first wall [1]. In a 2011 JET upgrade, Inconel was also used as a structural & substrate material in the construction of a new wall built to validate the use of metallic plasma-facing components [2]. This paper investigated a new manufacturing route based on nanosecond laser-processing to enhance the surface emissivity of Inconel 625 tiles to use as in-vessel calorimetry targets as part of the JET diagnostics system. Near perfect emissivity from Inconel 625 surfaces was achieved in the measured mid-wave infrared bad of ~3.2 – 4.7µm by tuning the laser surface processing parameters (fluence, frequency, and feed speed). It was proven that the achieved increase in emissivity was mostly caused by a combination of factors including microscale surface structures and a variable extent oxide layer. This paper presents for the first time a threefold increase of emissivity in Inconel 625 materials achieved via nanosecond laser processing in air. The functionalisation of Inconel 625 hereby presented could be useful for various industrial applications such as passive radiative cooling and thermal management of spacecraft.

Introduction

Emissivity (ε) describes the phenomenon of a material emitting thermal radiation from its surface, and is defined as the ratio of emitted thermal radiation compared to that of a black body (ε = 1) of the same temperature. Emissivity is a key parameter for interpreting surface temperature measurements made by infrared (IR) thermography. At the Joint European Torus (JET) magnetic confinement fusion experiment, IR thermography systems are one of the tools used to investigate distribution of heat loads from the fusion plasma to the device first wall [3] [4], which is a key area of investigation with implications for future fusion power device designs. It is desirable to use these IR thermography measurements to complement existing studies primarily based on data from thermocouples embedded in the machine wall components, in which the distribution of heat energy from the plasma could not be fully accounted for [5]. However, the JET in-vessel components consist

of tungsten, beryllium and Inconel surfaces[2] which have low emissivity and high reflectivity (note that for opaque materials the reflectivity r is related to emissivity by Kirchoff's radiation law as ε + r = 1). This makes accurate thermography measurements for energy balance studies very challenging, since infrared emission due to a small temperature increase of a surface can easily be swamped by reflections of infrared light from nearby, hotter surfaces. For this reason, a study was conducted to investigate design and manufacture of high emissivity, low-reflectivity "calorimeter tiles" suitable for the JET in-vessel environment, which could be installed in recessed positions (i.e. not directly in contact with the plasma) to provide improved IR thermography measurements, to better characterise diffuse energy loss channels from the plasma such as from radiation and neutral particles. Although no calorimeter tiles were ultimately installed in JET due to timeline and funding constraints of JET operations, here we report on the surface processing techniques successfully developed for this project.

Generally, emissivity of an object is affected by the material, its surface condition, temperature, radiation wavelength and direction of viewing. It is widespread practise to alter the emissivity of objects by adding a highly emissive layer such as a paint, an oxide, or a deposited thin coating [6][7][8][9][10]. These techniques generically increase emissivity by introducing substances with an intrinsically higher emissivity such as a ceramics or oxides, and by creating a textured surface by introducing fibres or similar macroscopic structures that have a high depth-to-width ratio (or aspect ratio).

Whilst some highly emissive coatings have been shown to work well in other vacuum and high heat applications [11][12], their performance and stability in the JET in-vessel environment was uncertain, and limited information about the exact composition and structure of commercial solutions was available to assess this further. The relevant operating conditions in JET include typically: high vacuum of ~10^{-4} Pa, temperatures of ~200 – 400C, exposure to ionised and neutral hydrogen species, and high fluxes of ionising radiation. Any degradation of the surface leading to release of material (either outgassing or delamination / break-up in to small solid pieces) could risk plasma operational performance by affecting the vacuum or plasma-facing surface conditioning, as well as degrading the thermography measurements themselves. It was therefore preferable to pursue the use of a material already qualified for the in-vessel JET environment, and increase the emissivity by geometrical modification of the surface, to minimise these risks.

The surface of metal components can be altered using additive manufacturing (AM) methods such as electron beam or laser beam melting/sintering, or subtractive manufacturing methods such as laser ablation/texturing. AM techniques are commonly used to produced textured surfaces for biomedical purposes [13] or to produce hydrophobic surfaces which, similarly to high emissive surfaces, can require microscopic features with high aspect ratios [14]. Pulsed laser ablation has been previously used to increase surface near-unity, broad band emissivity, addressing the limitations of other surface texturizing techniques that may produce narrowband or directional surface emissivity [15]. Aluminium was treated with a femtosecond laser source to produce mound-like microscale features with high aspect ratios, along with a thick oxide layer, both of which are attributed to an increase in hemispherical emissivity. Surface modifications of Inconel and similar nickel-based super alloys via laser ablation techniques has also been researched. Some of this research investigated laser ablation to reduce surface roughness [2, 16, 17], but others generally found that this treatment can produce microscale surface structures, some of which have relatively high aspect ratios. Cooling holes were machined through ceramic coated CMSX4 (nickel-based super alloy) using a femtosecond laser without causing significant collateral damage [18]. A study investigating laser shot peening (LSP) found that laser spot scanning produced column-like microstructure in the direction of the laser [19].

In another study, a femtosecond Ti:sapphire laser was used to study surface modification of Inconel 600, where morphological changes included the formation of crater-like features and creation of nano-aggregates and nano-structures [20].

Laser texturing of metal surfaces for extreme applications has revealed to be a successful technique for functionalising the materials' emissivity purely based on the formation of a thick oxide layer. However, to the best of authors' knowledge there is scarse information on laser texturing of Inconel materials and no research focused on using laser surface engineering or texturing on Inconel 625 to evaluate the possibility of using these materials as thermal emitters.

This paper details the investigation into using a nanosecond laser to ablate the surface of Inconel 625, creating microscale surface structures with high aspect ratio features to increase the hemispherical emissivity to at least 0.81; this is the typical hemispherical emissivity of carbon-fibre-composites (CFCs) that was another candidate material for JET calorimetry targets and was used as the plasma-facing material in JET until 2011.

This study attempts to demonstrate for the first time the effect of textures' geometry on the emissivity of Inconel 625 tiles by:

- The assessment of the geometrical changes post laser ablation in the areas of the JET Inconel 625 tiles.
- The identification of the characteristics of the nickel, chromium, iron and oxide extent at the laser ablated interface.
- An examination of the integrity of Inconel 625 substructure following laser ablation.
- The measurement of the emissivity post laser surface engineering.

2. Methodology

2.1 Samples

Cylindrical samples (30 mm diameter) were initially used for the main 3 sets of experiments (Figure 1). The final samples selected for the final processing were 5 Inconel plates, approximately 50x50mm with the central 40x40mm of the surface having been laser processed. Sample 3 had a processed area on both sides of the plate, in this case both sides have been measured and are denoted as samples 3a and 3b. All samples underwent ultrasonic cleaning with demineralised water and were air dried as would be performed for JET tiles before testing. Photographs of all samples are shown in the top row of **Figure 6**.

2.2 Advanced Laser processing of 625 Inconel plates

A 70 W Innolas MMS single mode SPI fibre laser (1060 nm wavelength) was used to laser process the initial samples and the final tiles. The computer numerically controlled (CNC) laser machine was operated in pulse mode and delivered pulses based on direct modulation of the seed laser allowing programmed waveforms. The waveforms are the results of an optimization of the peak power at a specific pulse repetition rate. At the waveform considered for the experiments the repetition rate for optimised peak power was 70 kHz, the pulse duration was 46 ns, and the maximum pulse energy was 1 mJ. Beam diameter at the focal points was measured to be approximately 29 µm. 3 sets of experiments were conducted to enable identification of ideal conditions for controlled emissivity samples. The selected factors (variables) were intensity, repetition frequency, feed speed and track distance. We also report the power density, however this is a variable dependent on intensity. Each

variable was studied at several levels (typically between two and eight), the values chosen for each parameter level are provided in Table 1. This resulted in a Taguchi L23 orthogonal array for experiment 1, L23 orthogonal array for experiment 2 and L28 orthogonal array for experiment 3.

Table 1. Laser processing parameter range.

Process parameters	Range exp 1	Range exp 2	Range exp 3
Intensity I (%)	10-20-30-40-50-60-70-80	30-40-50-60-80	40-60-70-80-90-100
Repetition frequency f (kHz)	20-35-60-85-100	25-35-45-85	35-85
Feed speed FS (mm s^{-1})	10-20-40-50-60-100-200	10-20-60-100	10-60-100
Track distance TD (µm)	20-40-60-80	10-20-30-40-60-80	1-6-8-10-20
Pulse duration τ (ns)	20-65-120-240	65-240	65-240
Power density (GW cm^{-2})	0.03-3.5	0.05-0.13	0.05-0.88
Number of times, R	1	1	1-4

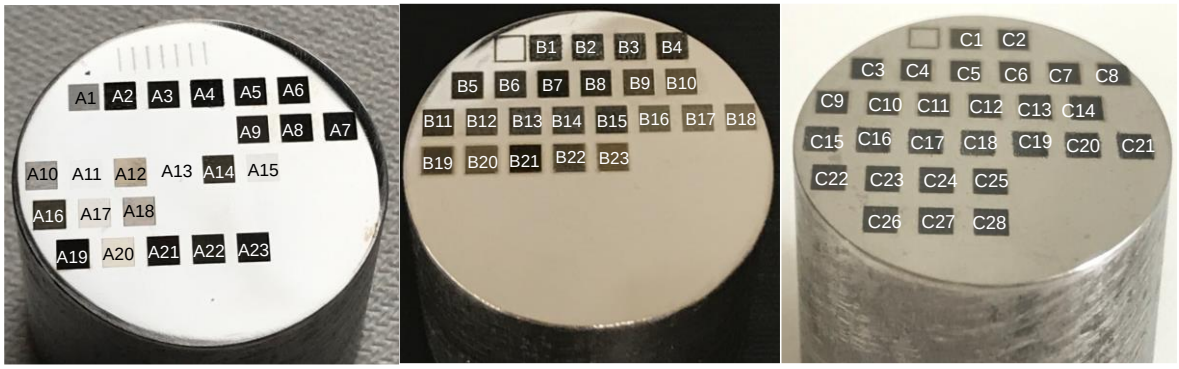

(a) (b) (c)

Figure 1: Photograph of the laser processed cylinders for the initial set of experiments: (a) experiment 1 - Taguchi L23 orthogonal array, (b) experiment 2 - Taguchi L23 orthogonal array, (c) experiment 3 - Taguchi L28 orthogonal array.

Following metrological and morphological evaluation of each 3 sets of experiments, the final set of 5 conditions were selected (Table 2) for laser processing on a set of larger samples as described in Section 2.1.

Table 2: laser parameter range used in the various experiments.

Process parameters	Frequency (kHz)	Feed speed (mm s^{-1})	Track distance (µm)	Pulse duration (ns)	Laser Fluence (J/cm2)	Energy Density (GW/cm2)	Number of times
1	35	100	0.01	65	45.76	0.70	1
2	35	100	0.001	65	45.76	0.70	1
3a	35	100	0.01	65	37.18	0.57	1
3b	35	100	0.01	65	57.20	0.88	1
4	85	100	0.01	240	16.48	0.07	4
5	35	60	0.01	240	22.88	0.09	4

2.3 Material characterisation

2.3.1 Metrological analysis

An Alicona Infinite Focus, 3D white light interferometer was used with a vertical resolution of 110 nm and lateral resolution of 2.13 µm allowing the topographical analysis of the laser processed areas before and after testing. Using ISO 13565, an Abbott-Firestone's curve was plotted for each sample, and the 2D roughness parameter Ra was extrapolated from each curve. Using ISO 25178, Abbott-Firestone's curve was plotted relatively to the entire surface and the 3D counterpart Sa was also derived.

2.3.2 Subsurface integrity evaluation

All laser processed samples were cleaned in a water-filled ultrasonic bath (30 minutes) to remove any debris. A JEOL Zeiss Scanning Electron Microscope (SEM) was used to perform imaging and chemical composition using energy dispersive X-ray spectroscopy (EDS). Images were taken at x150, x1000 and x10000 of as-received and laser processed areas to allow benchmarking. A Focus ion beam milling machine Nova 600 NanoLab Ga DualBeam was used to cut cross sections of the laser processed areas for analysis. A protective platinum layer (2 - 10 µm thick) was coated on the area to be milled to avoid damage to the subsurface. The cross-sectioned structures were analysed using energy-dispersive X-ray spectroscopy (EDS) to quantify changes in chemical composition and measure the average thickness of the oxide layer and the mound composition (Table 5).

2.4 Emissivity measurements

2.4.1 IR Camera & Calibration

The emissivity of the samples was determined by observing them with an IR camera while heating them over a temperature range of around 100°C and comparing the measured increase in IR radiance with that of a commercial high emissivity reference source.

This yields a single value of the directional spectral emissivity, in this case averaged over the wavelength range ~3.2 – 4.7 µm and a solid angle of ~1.7×10^{-3}sr in a direction ~40° from the surface normal. In the rest of this document this will simply be referred to as the emissivity and denoted ε.

The IR camera used was based on a cooled 640x512 pixel InSb focal plane array (SCD Pelican-D) with a CEDIP 50mm mid-IR lens, operating at f/3 (limited by the detector cold stop) and with a band pass interference filter installed in the camera to define the measurement wavelength band. The overall spectral response curve of the camera setup is shown in ***Figure 2***.

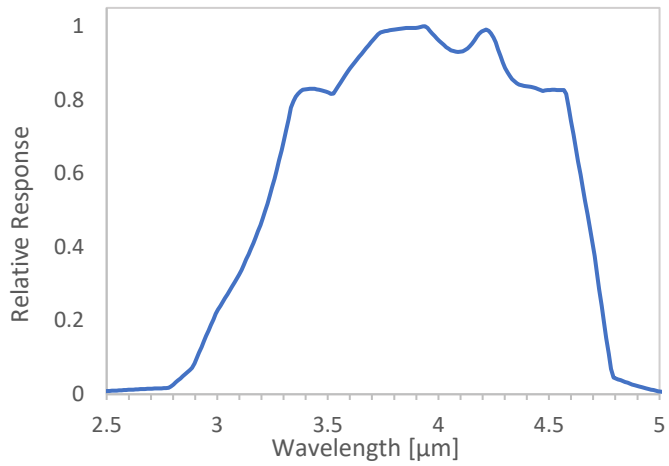

Figure 2: Spectral response curve of the camera used for IR measurements.

Correction of per-pixel gain variations and lens vignetting was performed by imaging a uniform flat surface at two different temperatures (an Electro-physics brand "NUC plate" heated on the same hot plate as the samples), resulting in two images S_{hot} and S_{cold}. The relative sensitivity of the i^{th} detector pixel was then calculated as $G_i = \frac{S_{\mathrm{hot,i}} - S_{\mathrm{cold,i}}}{\overline{S_{\mathrm{hot}} - S_{\mathrm{cold}}}}$, where the overbar denotes a mean over all pixels.

Detector offsets and stray IR light from the environment were removed by always working with difference images created by subtracting frames taken with the sources at different temperatures. Dividing the difference image by the calculated gains, i.e. as $S(T_2, T_1) = (S_{T_2} - S_{T_1})/G$ then gives an image with uniform response for all pixels and the background removed.

The value of the difference image between two temperatures T_1 and $T_2$for an object with emissivity ε, assuming the emissivity is constant over the temperature interval and observed wavelength range, is given by:

$$S(T_2, T_1, \varepsilon) = \varepsilon\, C \left(\int L(T_2, \lambda)\; R(\lambda)\, \mathrm{d}\lambda - \int L(T_1, \lambda)\; R(\lambda)\, \mathrm{d}\lambda \right) \qquad (1)$$

Where $L(T, \lambda)$ is the black body spectral radiance at temperature T and wavelength λ given by Planck's law, $R(\lambda)$ is the camera spectral response curve (shown in ***Figure 2***) and C is a calibration factor accounting for the etendue and transmission of the observing optics, detector quantum efficiency, digitisation gain and camera exposure time.

Calibration of the IR camera setup was performed by imaging a commercial high emissivity reference source (Isotech Pegasus-R , $\varepsilon = 0.995$ nominal) at 5 different temperatures. The lowest temperature was used as the reference temperature T_1 for all images. For each temperature setting of the source, the term in brackets in equation 1 was calculated, and a linear fit of the measured $S(T_2, T_1)$ as a function of the term in brackets was used to determine the value of εC. Assuming $\varepsilon = 0.995$, the obtained value of the calibration constant was $C = 322\ \mathrm{W^{-1}m^2sr^1}$ for a camera integration time of $\tau = 1\mathrm{ms}$, which was used throughout this experiment.

2.4.2 Sample heating & observation setup

The samples were heated from the back (non-processed side) on a hot plate to achieve a uniform temperature across the sample surface, and the temperature of the top (camera-facing) surface was monitored with a K-type thermocouple attached to the un-treated Inconel surface in 1 corner of the plate, with a thin (<0.5mm) layer of thermal interface material used to obtain good thermal contact between the thermocouple and sample surface. This thermocouple was read with a hand-held meter with a precision of 1°C. The IR camera observed the samples at an angle of approximately 40° to the sample surface normal. Photographs of the experimental setup are shown in **Figure 3**.

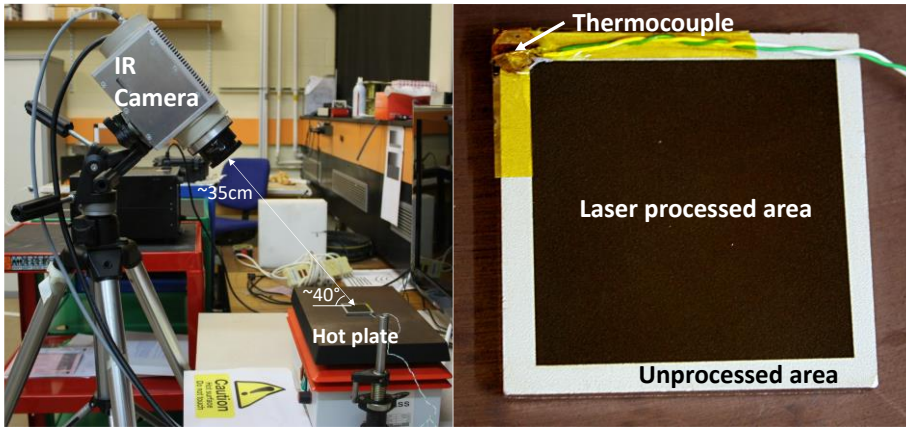

Figure 3: a) observation and heating setup; (b) Location of the samples with thermocouple attached.

Each sample was heated from room temperature to around 115°C using the hot plate, during which time the thermocouple measurements and IR images were recorded at 1 minute intervals. This resulted in a time series of camera images and corresponding time series of surface temperatures from the thermocouple.

2.3.3 Emissivity Calculation

For each sample, the average of 5 camera images before the heating started (i.e. with the sample at room temperature) was used as the T_1 reference, with the value of T_1 measured from the thermocouple. For subsequent IR images, the camera signal which would correspond to a black body i.e. $\varepsilon = 1$ was calculated from equation 1 as $S_{BB} = S(T_{\mathrm{TC}}, T_1, 1)$, where T_{TC} is the thermocouple measurement at the time of the camera image being recorded. Three regions of interest in the images were chosen, and the mean camera signal in each region S_{ROI} calculated for each recorded image: (1) an ROI covering the entire laser processed sample surface, (2) a small ROI of approximately cm on the closest part of the treated surface to the thermocouple, and (3) an ROI on the un-processed Inconel surface on the border of the piece. An example showing these ROIs as shaded regions on an IR image of sample 1 is shown in ***Figure 4***. The purpose of measuring a small ROI near the thermocouple in addition to averaging over the treated surface is to compare this result with the large ROI, with any large difference indicating undesired non-uniformity of the emissivity, sample temperature or measurement setup. The average emissivity of the surface in each ROI was then determined from the slope of a linear fit of S_{ROI} as a function of S_{BB}.

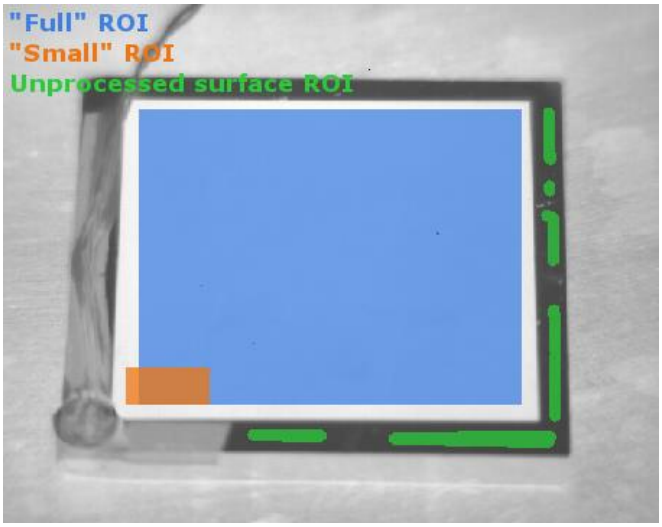

Figure 4: Example IR image of sample 2 showing the different regions of interest for emissivity measurement.

3. Results

3.1 Emissivity response of Inconel 625 tiles

A plot of measured radiance S_{ROI}/C vs black body radiance S_{BB}/C for all measured samples is shown in Figure 5. The filled symbols on the plot represent data from the ROI covering the whole laser processed area, while un-filled symbols are for the unprocessed Inconel surface. The small ROI data is not shown on the plot to aid clarity, since it would largely overlap with the full ROI data. A good linear relationship is obtained between S_{ROI} and S_{BB} in all cases; the emissivity of the un-treated surface is clearly very consistent between all samples at around 0.3, and that all but one of the samples (Sample 3) have emissivity > 0.9 on the processed surface.

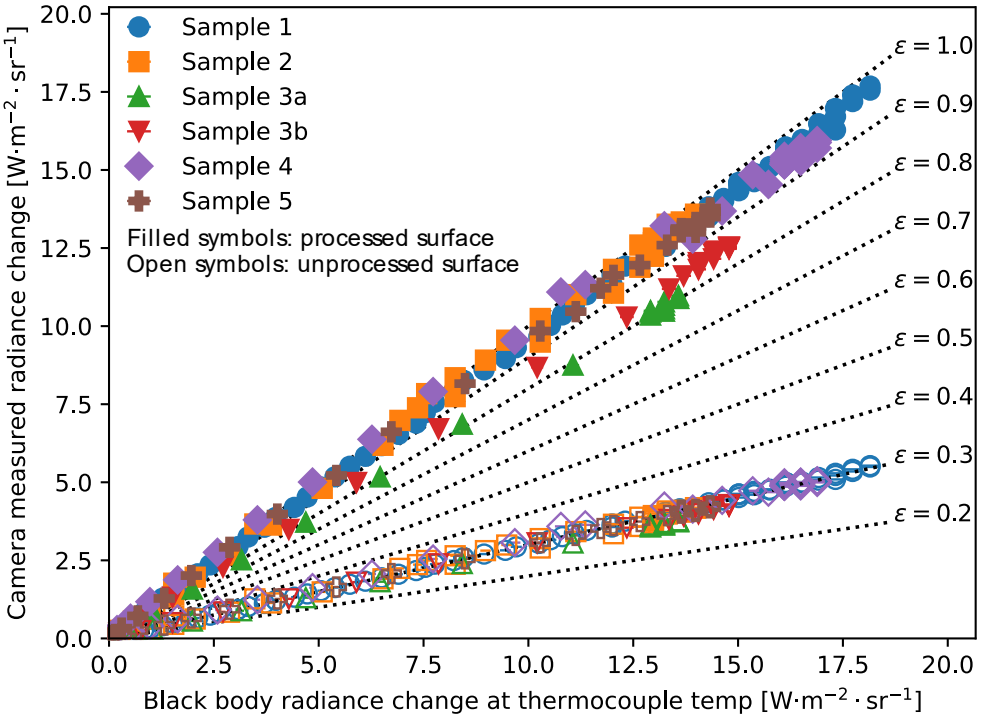

Figure 5: Measured IR radiance from samples (vertical) compared to that expected from an ideal black body (horizontal). Filled symbols correspond to the "Full ROI" on the treated surface, un-filled symbols correspond to the un-treated surface. Black dashed lines correspond to different emissivity values.

The fitted values of emissivity are provided in Table 3. The fitting errors on the emissivity are around 0.002 in all cases; this is unlikely to be the dominant source of error, so here the emissivity values have been rounded to 2 digits.

Table 3: Fitted emissivity values for the measured samples.

Sample	Fitted ε value		
	Processed surface, "Full ROI"	Processed surface, "Small ROI"	Unprocessed surface
1	0.96	0.91	0.30
2	0.97	0.95	0.29
3a	0.80	0.78	0.28
3b	0.85	0.83	0.29
4	0.93	0.91	0.30
5	0.95	0.92	0.29

All samples except 3a exceed the requirement of $\varepsilon \geq 0.81$, with samples 2, 1 and 5 having the highest emissivity. The emissivity of the un-coated surfaces is very consistent between all samples which is a good indication of the consistency of the adopted measurement technique, with a mean value across all samples of $\varepsilon = 0.29$.

The fitted emissivity values for the smaller ROI are consistently slightly lower than for the full ROI. This can be understood by looking at examples of the individual camera images normalised to the expected black body brightness to give an emissivity "image", in the lower row of Figure 6, which

shows some variation of the apparent emissivity over the sample surfaces. In some cases, particularly samples 2 and 3, the variation seen in the emissivity images reflects patterns visible on the treated surface in visible light. Such a correlation is not clearly visible on samples 1, 4 and 5, so it is less clear whether the variations seen across the surface for these is due to variation of the surface or measurement effects such as non-uniformity of the plate heating or uncorrected structure in the camera response.

From Figure 6, although sample 2 showed the highest measured emissivity, it also presented significant marking of the surface, presumably resulting from handling of the sample post surface processing, despite being subject to similar handling as all the other samples. Note also that the significantly lower emissivity of sample 3 is reflected in the visual appearance of the processed surface as a lighter grey than for the other samples (Figure 6 top), which is consistent with what would be expected. Based on the emissivity images and differences between the small and large ROI results, Samples 4 and 5 show the best uniformity of the high emissivity over the treated area.

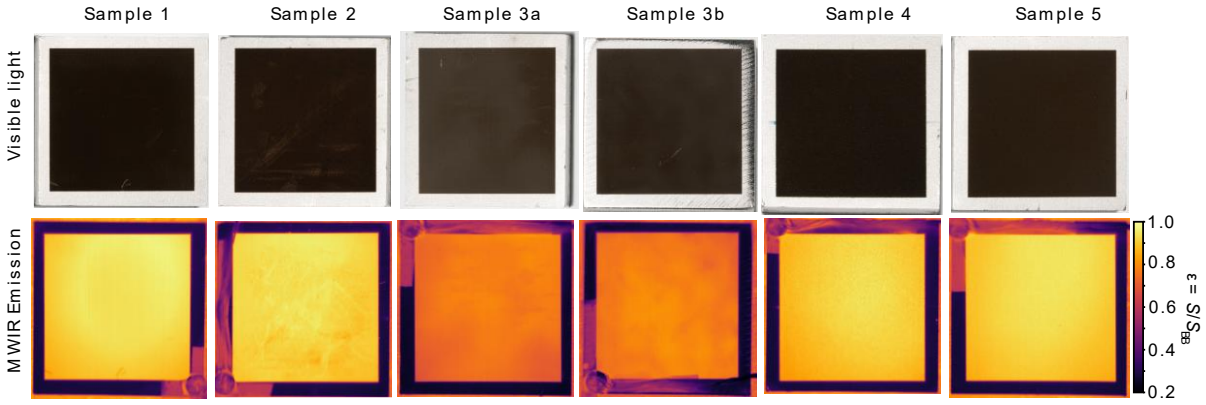

Figure 6: Top row - visible light photographs of the samples (fixed exposure for all samples). Bottom row: IR emission images from each sample normalised to black body radiance at the same temperature.

3.2 Assessment of the topographical changes post laser processing

Plots of the 3D surface roughness Sa for benchmark and all post processed samples are reported in Figure 7. A strong variability of surface roughness was purposely designed and achieved to evaluate the effect this could have on emissivity values. Highest Sa post process was achieved for samples 4 and 5. Although lower energy and longer pulse were used for these processing conditions, due to the high number of scans/repetitions a more aggressive ablation was executed on these two samples. Two defined groups of emissivity are evident in graph in Figure 8, one including samples (3a and 3b) with emissivity below 0.86 and the other including samples (1, 2, 4 and 5) with emissivity values above 0.9 which in turn corresponds to values of Ra and Sa below and above 10 µm. The graphs in Figure 8 show a clear relationship between roughness and emissivity and the primary effect of change of surface roughness particularly when this exceeds 10 microns (Ra and Sa). It can be noticed that those trends are also similar for the 3D surface roughness values Sa except for sample 4 in which the dependency is not direct. This could be attributed to a secondary effect introduced by the formation of oxides: in sample 4 formation of oxides is within the subsurface while in sample 5 this is only superficial (Figure 12).

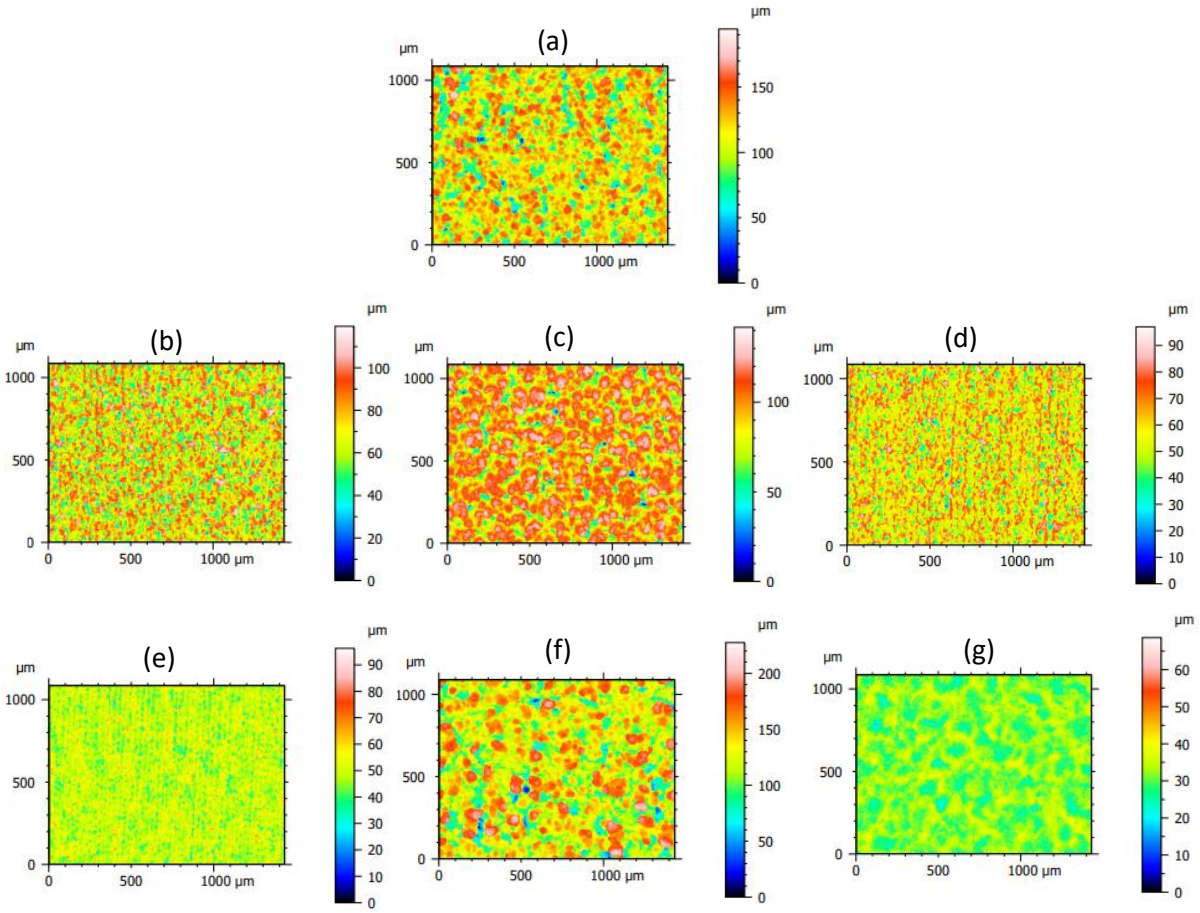

Figure 7: Mapping data of 3D surface roughness Sa measured based on ISO 25178 for: a) as-received, b) sample 1, c) sample 2, d) sample 3a, e) sample 3b, f) sample 4, g) sample 5.

Table 4: 2D and 3D surface roughness of benchmark and post processed samples measured using ISO 13565 and ISO 25178.

Sample	$R_a$pre-process	R_a post-process		S_a	
	R_{a1} (µm)	$Mean$ (µm)	$Std\ dev$ (µm)	$S_a\ pre\ process$ (µm)	$S_a\ post\ process$ (µm)
1	2.204	11.253	1.450	2.627	13.040
2	2.263	13.311	1.572	2.630	15.082
3a	2.121	7.087	1.452	2.648	9.006
3b	2.118	3.347	0.291	2.547	4.051
4	2.172	13.954	6.904	2.689	24.353
5	2.364	15.313	0.763	2.595	19.808

Highest emissivity was seen in sample 2, followed by sample 1, 5 and 4. Samples 2 and 1 presented with a minimal difference in emissivity (0.01), however mapping of the 3D surface roughness data (Figures 7b and c) clearly indicates different aspect ratios for the two samples. In terms of micro-topography, the achieved textures resemble shark skin for sample 2 while in sample 1 micro agglomerates less than 50 µm wide are present (Figure 8). It should be noticed that the only change in processing conditions between these two samples is the track-distance. This was reduced by 10 times (1 nm for sample 2) in the sample showing the highest measured emissivity.

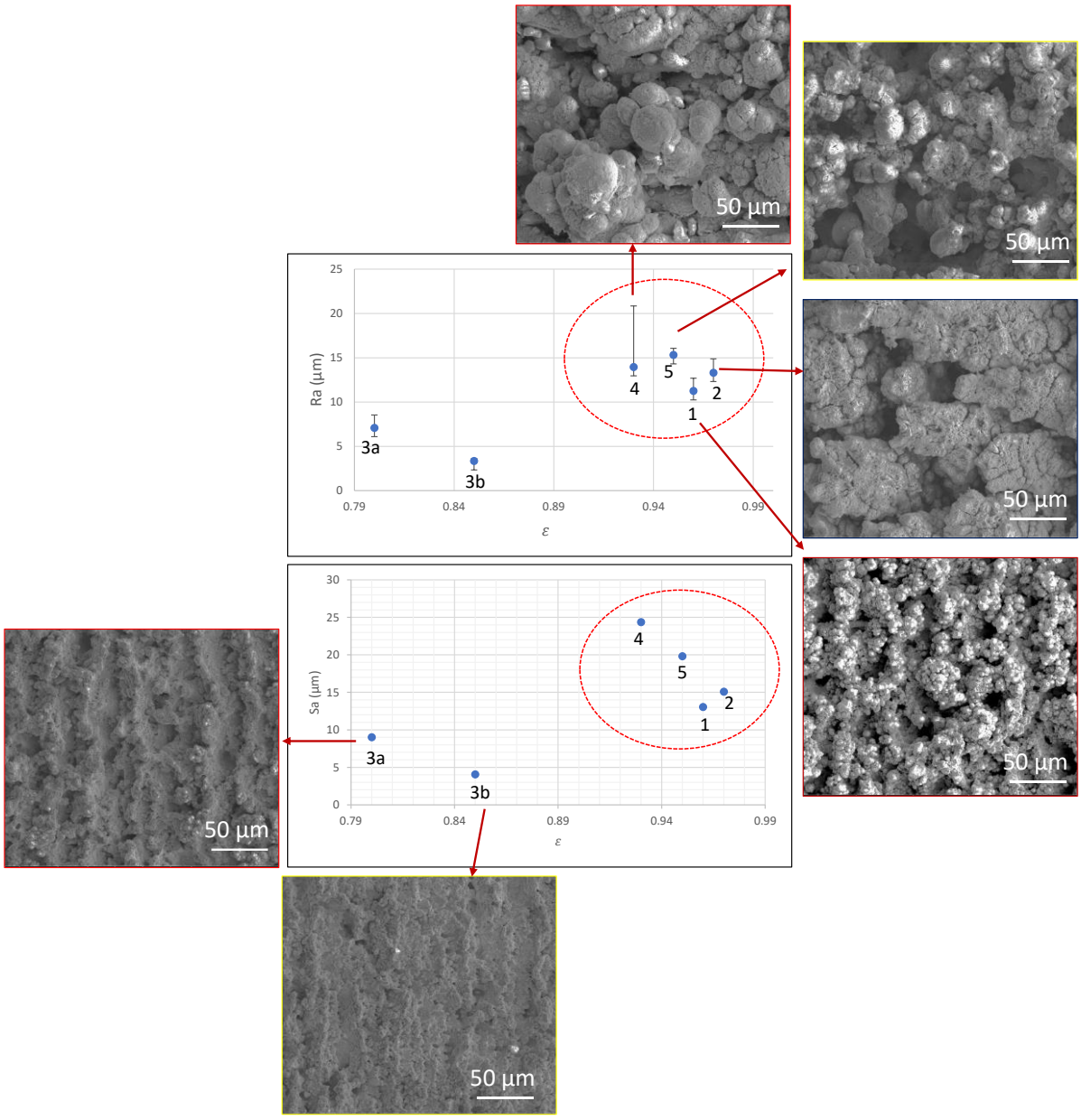

Figure 8: plots of 2D and 3D surface roughness versus emissivity, the SEM images are representatives of each sample numbered in the graph.

3.3 Evaluation of subsurface integrity post processing

An important part of this study aimed at evaluating the effect of oxide formation and surface textures geometry on the measured emissivity. Previous research already demonstrated that spectral emissivity of various oxidized metals is higher than the un-oxidized reference samples at low wavelengths. However, this range was found to widen when exposure time increases and therefore oxide layer grows thicker. This study also found that the effect of roughness change on emissivity was lower than the effect of surface oxidation [21].

As the laser processing was conducted in air, a certain extent of oxide formation is present in all processing conditions. However, there doesn't seem to be a direct relation between oxygen content and increased emissivity. It is likely that a combination of effects would have contributed to the threefold increase in emissivity including surface topography and surface chemistry. From the emissivity measurement results there are two main contributing factors to the increase of emissivity in Inconel 625: formation of an oxide layer formed using LSP in air, and microscale surface roughness. In this study surface topography seems to have a dominant effect. This disagrees with previous work from Jo et al. who found that the effect of roughness change on emissivity was lower than the effect of surface oxidation [21].

A Focused Ion Beam cross section of the benchmark sample with an EDS of its chemical components is represented in Figure 10. This should serve as a comparison with the post processed samples in Figure 9. The pre-processed sample appears rough (Ra = 2.2 ± 0.1 µm) but with a homogeneous structure of its characterising chemical components, Cr, Fe and Ni. Pt was used in the FIB process to stabilise the sample while preparation occurred.

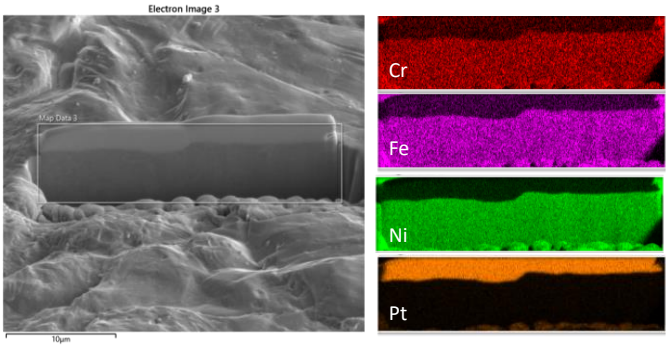

Figure 9: SEM images of Focus Ion Beam milled Inconel 625 benchmark sample.

All samples were laser processed in air and, as such, oxygen formation was expected. All samples in fact were presented with a certain amount of oxygen which appeared post process. A certain amount of nickel nanoparticles was also deposited on the surface post ablation. These latter become oxidised and it was found that the layer of oxidised nanoparticles is proportional to the increase of fluence (Table 2). The oxide that builds up on the surface structures reported is likely in the form of oxidized nanoparticles that are created because of the laser ablation and deposited on the surface after each laser pulse, like the development of aggregated nanoparticle spheres that form using FLSP at low fluences on metals.

Chemical composition analysis via EDS measurements (Table 5) revealed a reduction of Ni content for all samples that showed highest emissivity (1, 2, 4 and 5) and an increase in Ni for samples 3a and 3b. For benchmark initial composition was 45.9% Ni, and Cr at 12.7%. Chromium content seems to have remained unchanged for samples 3a and 3b while this reduced for samples 1, 2 and 5. Sample 4 revealed a twofold increase of Cr %, a threefold reduction of Ni % and the highest oxygen content measured at 24.7 %. Samples 3a and 3b, with lowest oxygen content measured at 2.5% and 0.9% respectively still produced emissivity of 0.8 to 0.85, therefore an increase of emissivity is reported even when the effect is only attributed to surface texture modification.

Table 5: EDX spectra for benchmark and laser processed samples.

Sample	Map sum spectrum (wt%)				
	Ni	Fe	Cr	C	O
Benchmark	45.9	7.3	12.7	/	/

1	33.6	5.9	6.7	6.8	10.8
2	30	5.6	8.6	5.5	16.2
3a	56.1	7.6	13.8	4.0	2.5
3b	59	8.2	14.0	3.7	0.9
4	18.1	6.3	23.8	4.2	24.7
5	50.4	7.8	9.4	3.7	9.1

Redeposited Nickel was seen for all laser processed conditions. Pockets of redeposited nickel coated with oxygen (10.8%) with an average thickness of around 2 microns were revealed in condition 1 (Figure 10a). EDS analysis of condition 2 (Figure 10b and Figure 12b) showed a 10 µm thick layer of oxygen (16.2%) just below the protective Pt layer. Conditions 3a and 3b (Figure 10c-d) revealed, similarly to condition 1, pockets of redeposited nickel (56.1% for 3a and 59% for 3b) coated in oxygen, with a lower %, 2.5 and 0.9% respectively for 3a and 3b. FIB cross section of sample processed in condition 4 showed the highest oxidation (24.7%) and a very different morphology compared to other processing conditions. The onion-like structure (Figure 10e) presented with rings of chromium (23.4%) and nickel (18.1%) alternating with intermittent oxygen layers (Figure 11e and Figure 12e). Large areas of nickel growth were identified processing at condition 5, a very thin layer of oxygen (2 µm) was also deposited due to the surface processing in air (Figure 10f, Figure 11f and Figure 12f).

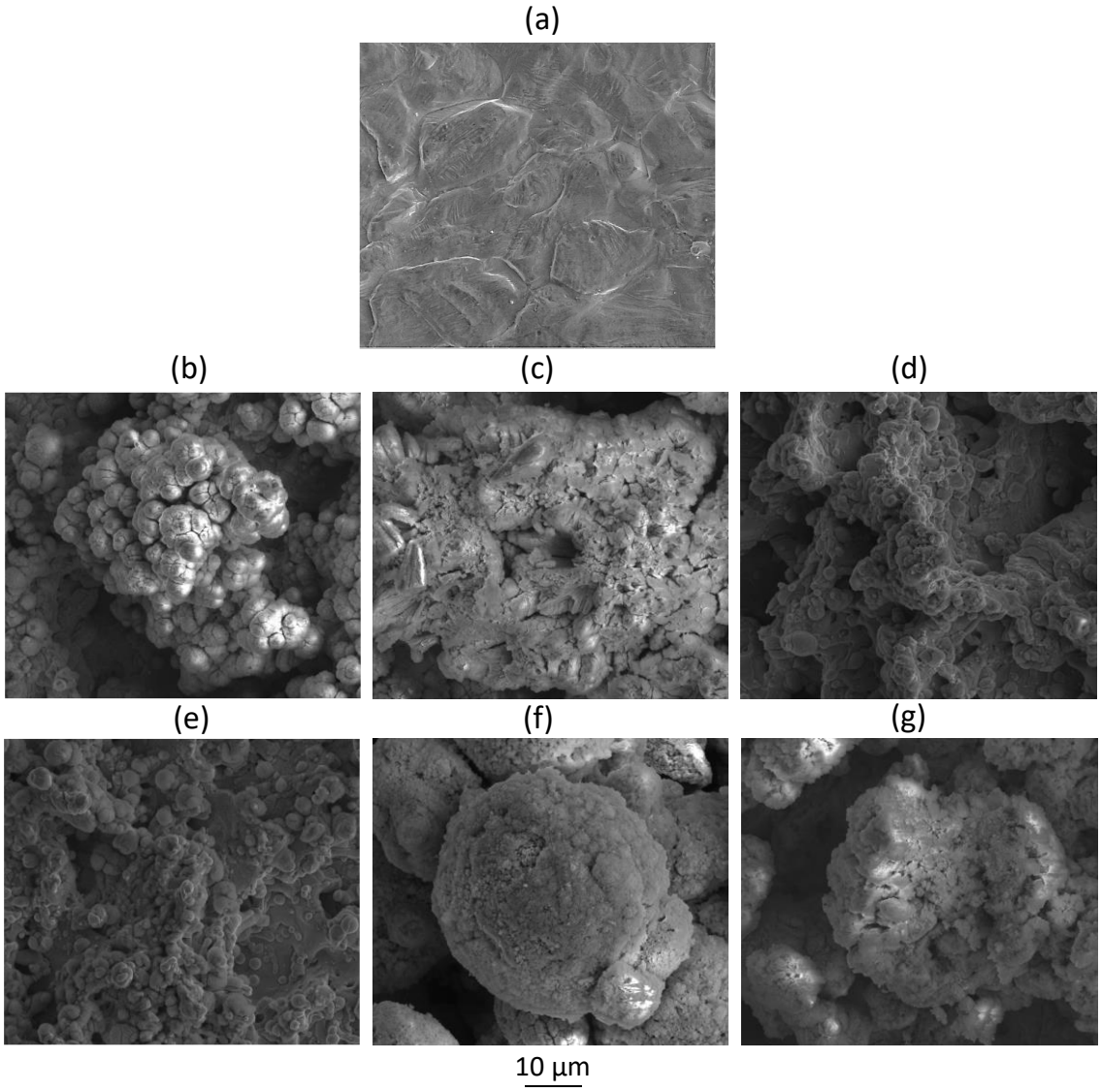

Figure 10: SEM images of Inconel 625 samples processed at various process parameters as described in Table 2: a) as-received, b) sample 1, c) sample 2, d) sample 3a, e) sample 3b, f) sample 4, g) sample 5.

Previous research on periodical micro-grooving showed that there is a strong impact of geometry on emissivity and that V shaped grooves performed better than hemispherical or rectangular features [21]. This effect is independent of oxides formation; however, oxidation (when present) generally increases the surface roughness of the surface layer and creates an interference effect which can further enhance surface emissivity. It has been previously demonstrated that high chromium content metals show a limited oxide layer growth for austenitic alloys [23], this means that for the highest chromium containing post processed sample (condition 4) it is less likely that the high emissivity result is due to the oxide layer formation but rather resulting from the change in topography.

Using a track distance of 10 nm (condition 1) produced extremely small nickel micro- agglomerations (in the order of 5 µm). These are surrounded by a layer of oxygen (Figure 11a and Figure 12a). When the track-distance is reduced even further (up to 1 nm in condition 2) then larger nickel flakes formed (cross section 20 µm by 10 µm). These were again surrounded by oxygen (Figure 11b and Figure 12b).

The morphologies of samples 4 and 5 are quite different. In sample 4 a higher repetition rate and longer pulse caused formation of an onion-like structure with characteristic rings of chromium, nickel, and oxygen (Figure 11e). A previous study [22] demonstrated that any process causing grain refinement would facilitate the outward diffusion of chromium promoting Cr2O3 scale growth, but also enhancing the inward diffusion of oxygen (Figure 11e).

In sample 5 extra-large nickel areas (cross section 20 µm by 20 µm) surrounded by pockets of chromium and coated in oxygen are visible in Figure 11f and Figure 12f. As the morphology of these two is quite different the major factor in contributing to an enhanced emissivity should be found in the surface roughness Sa, which was 24.353 µm for sample 4 and 19.808 µm for sample 5 and noticeably higher than for all the other processed samples. This is also in accordance with emissivity results for samples 3a and 3b which showed the lowest increase of emissivity as well as the lowest surface roughness (respectively 9.006 µm and 4.051 µm).

Of the final samples produced, the surface processing conditions of Samples 4 and 5 appear to be the most preferable for creating dark tiles, due to the combination of high emissivity, good uniformity, and robustness to handling of the treated surface.

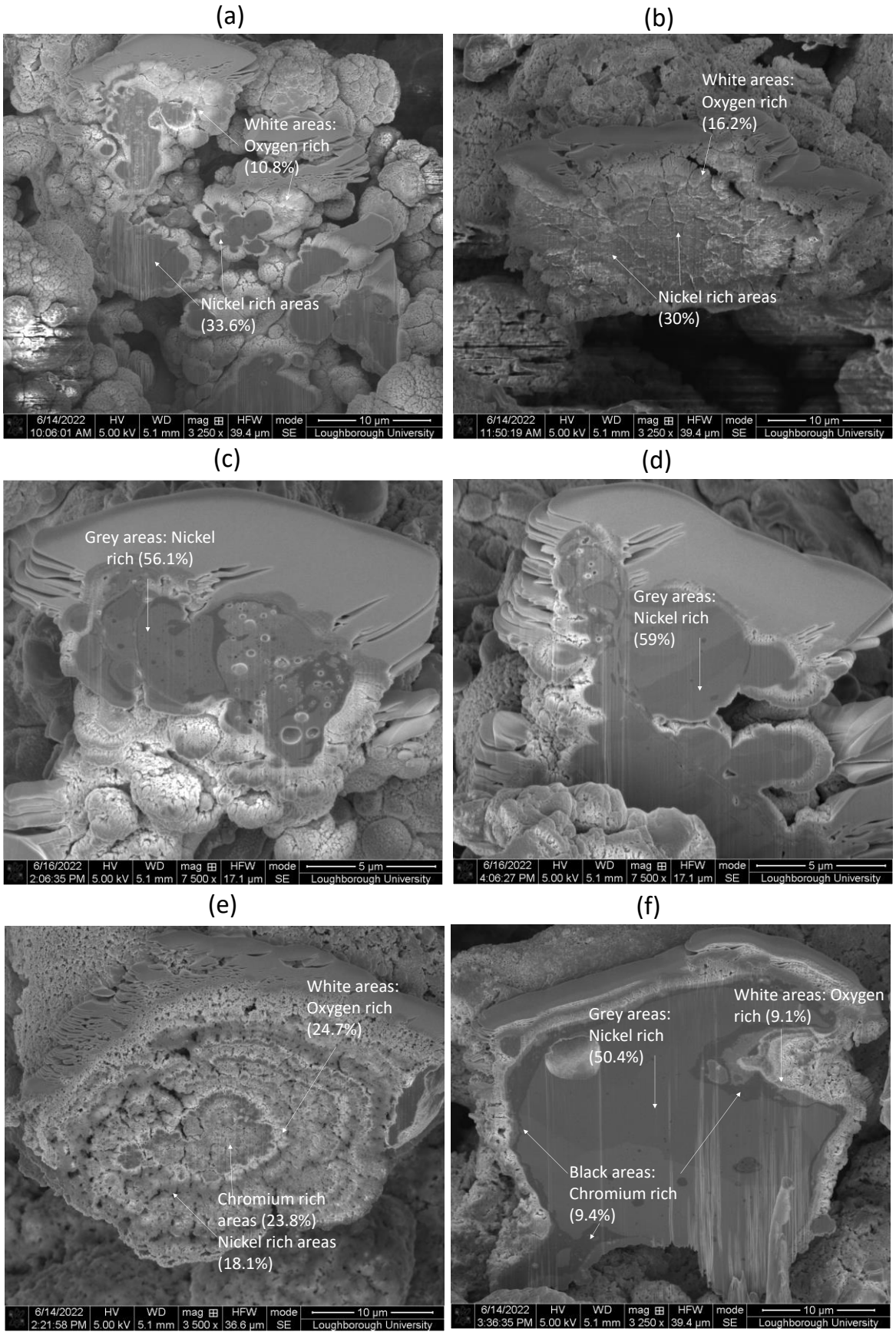

Figure 11: FIB images of Inconel 625 samples processed at various laser conditions as reported in Table 2: a) sample 1, b) sample 2, c) sample 3a, d) sample 3b, e) sample n 4, f) sample 5.

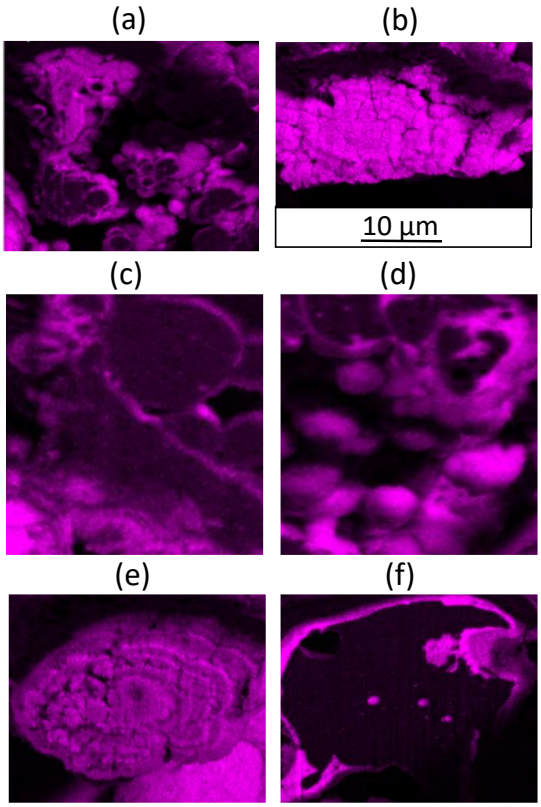

Figure 12: EDX map of the post process samples showing the oxide formation at different processing parameters*:* FIB images of Inconel 625 samples processed at various laser conditions as reported in Table 1: a) sample 1, b) sample 2, c) sample 3a, d) sample 3b, e) sample 4, f) sample 5.

4. Conclusions

Based on the emissivity results obtained, laser processing of Inconel materials can produce high emissivity surfaces exceeding the emissivity of carbon tiles, i.e. exceeding the stated requirements on optical properties for the JET black tiles project. Of the final samples produced, the surface processing conditions of Samples 4 and 5 appear to be the most preferable for creating dark tiles, due to the combination of high emissivity, good uniformity, and robustness/stability to handling of the treated surface. Two main contributing factors were found to increase the emissivity in Inconel 625: formation of an oxide layer formed using LSP in air, and microscale surface roughness. In this study surface topography seems to have a dominant effect. Chemical composition analysis revealed a reduction of nickel content for all samples that showed highest emissivity (1, 2, 4 and 5) and an increase in nickel for samples 3a and 3b. Samples 3a and 3b, with lowest oxygen content measured at 2.5% and 0.9% respectively still produced emissivity of 0.8 to 0.85, therefore an increase of emissivity is reported even when the effect is only attributed to surface texture modification.

It is reported for the first time on Inconel 625 materials that the achieved best performing surfaces (emissivity in the range 0.93-0.97) have higher emissivity than industrial coatings or metamaterials. LSP in the nanosecond regime has proven to be a fast and low-cost technique to functionalise Inconel 625 surfaces and for the manufacture of high thermal emitters.

Acknowledgements

This work, which has been carried out partly within the framework of the Contract for the Operation of the JET Facilities up to 31 October 2021, has been funded by the Euratom Research and Training Programme. Since 31 October 2021, UKAEA has continued to work with the EUROfusion Consortium as an Associated Partner of Max-Plank-Gesellschaft zur Förderung der Wissenschaft e.V represented by Max-Plank-Institut fur Plasmaphysik ("IPP") pursuant to Article 9.1 of the EUROfusion Grant Agreement for Project No 101052200. The views and opinions expressed herein do not necessarily reflect those of the European Commission. JET, which was previously a European facility, is now a UK facility collectively used by all European fusion laboratories under the EUROfusion consortium. It is operated by the United Kingdom Atomic Energy Authority, supported by BEIS and its European partners.

References

[1] Hirai, Takeshi & Linke, Jochen & Sundelin, P & Rubel, M. & Kühnlein, W & Wessel, E & Coad, J. & Lungu, Cristian & Matthews, G. & Pedrick, L & Piazza, G. & Contributors, Jet-Efda (2007). Characterization and heat flux testing of beryllium coatings on Inconel for JET ITER-like wall project. Phys. Scr. T128.

[2] Romanelli, F. 'Overview of the jet results with the ITER-like wall', Nuclear Fusion, 53(10):104002 (2013).

[3]E. Gauthier, H. Roche, E. Thomas, S. Droineau, B. Bertrand, J.B. Migozzi, W. Vliegenthart, L. Dague, P Andrew, T. Tiscornia, D. Sands, JET-EFDA Contributors. ITER-like wide-angle infrared thermography and visible observation diagnostic using reflective optics. Fus. Eng. Des. 82 (5-14) (2007).

[4] Balboa, I. G Birkenmeier, E R Solano, I S Carvalho, J C Hillesheim5, E Delabie, E Lerche Taylor, D Gallart, M J Mantsinen, C Silva, C Angioni, F Ryter, P Carvalho, M Fontana, E Pawelec, S A Silburn, P Sirén, S Aleiferis, J Bernardo, A Boboc, D Douai, P Puglia, P Jacquet, E Litherland-Smith, I Jep, D Kos, H J Sun, A Shaw, D King, B Viola, R Henriques, K K Kirov, M Baruzzo, J Garcia, A Hakola, A Huber, E Joffrin, D Keeling, A Kappatou, M Lennholm, P Lomas5, E de la Luna, C F Maggi, J Mailloux, M Maslov, F G Rimini, N Vianello, G Verdoolaege, H Weisen. The role of isotope mass and transport for H-mode access in tritium containing plasmas at JET with ITER-like wall. Plasma Phys. Control. Fusion 65 064005 (2023).

[5] Matthews, G. F. et. al. 2017 Nucl. Mater. Energy 12: 227-233.

[6] Brandt, R., Bird, C. and Neuer, G., 2008. Emissivity reference paints for high temperature applications. *Measurement*, 41(7): 731-736 (2008).

[7] Streyer, W., Law, S., Rooney, G., Jacobs, T. and Wasserman, D. Strong absorption and selective emission from engineered metals with dielectric coatings. *Optics Express*, 21(7): 9113 (2013).

[8] Group, S., 2022. *Elevated-Temperature, Highly Emissive Coating for Energy Dissipation of Large Surfaces*. [online] Techbriefs.com. Available at: <https://www.techbriefs.com/component/content/article/tb/pub/briefs/materials/19903> [Accessed 20 May 2022].

[9] Acktar black coatings. 2022. *How to Increase Surface Emissivity - Acktar black coatings*. [online] Available at: <https://www.acktar.com/how-to-increase-surface-emissivity/> [Accessed 20 May 2022].

[10] Song, J., Hao, X., Yuan, Z., Liu, Z. and Ding, L. Research of Ultra-Black Coating Emissivity Based on a Controlling the Surrounding Radiation Method. *International Journal of Thermophysics*, 39(7) (2018).

[11] Haupt, K., 2022. *Plasma physics | Be clean, be strong*. [online] ITER. Available at: <https://www.iter.org/newsline/-/2977> [Accessed 20 May 2022].

[12] Spilker, B., Linke, J., Loewenhoff, T., Pintsuk, G. and Wirtz, M. Performance estimation of beryllium under ITER relevant transient thermal loads. *Nuclear Materials and Energy*, 18, pp.291-296 (2019).

[13] Bose, S., Robertson, S. and Bandyopadhyay, A. Surface modification of biomaterials and biomedical devices using additive manufacturing. *Acta Biomaterialia*, 66, pp.6-22 (2018).

[14] Davoudinejad, A., Cai, Y., Pedersen, D., Luo, X. and Tosello, G. Fabrication of micro-structured surfaces by additive manufacturing, with simulation of dynamic contact angle. *Materials & Design*, 176: 107839 (2019).

[15] Reicks, A., Tsubaki, A., Anderson, M., Wieseler, J., Khorashad, L., Shield, J., Gogos, G., Alexander, D., Argyropoulos, C. and Zuhlke, C. Near-unity broadband omnidirectional emissivity via femtosecond laser surface processing. *Communications Materials*, 2(1) (2021).

[16] M Pacella, D Brigginshaw, 2020. Enhanced wear performance of laser machined tools in dry turning of hardened steels. Journal of Manufacturing Processes, 56, 189-196: 10 (2020).

[17] KE Hazzan, M Pacella, TL See. Understanding the surface integrity of laser surface engineered tungsten carbide. The International Journal of Advanced Manufacturing Technology, 1-23 (2022).

[18] Das, D. and Pollock, T. Femtosecond laser machining of cooling holes in thermal barrier coated CMSX4 superalloy. *Journal of Materials Processing Technology*, 209(15-16): 5661-5668 (2009).

[19] Bugayev, A., Gupta, M. and Payne, R. Laser processing of inconel 600 and surface structure. *Optics and Lasers in Engineering*, 44(2), pp.102-111 (2006).

[20] Stasic, J., Gakovic, B., Krmpot, A., Pavlovic, V., Trtica, M. and Jelenkovic, B.. Nickel-based super-alloy Inconel 600 morphological modifications by high repetition rate femtosecond Ti:sapphire laser. *Laser and Particle Beams*, 27(4), pp.699-707 (2009).

[21] HangJin J,. King J L, Blomstrand K, Sridharan K. Spectral emissivity of oxidized and roughened metal surfaces. International Journal of Heat and Mass Transfer 115: 1065–1071 (2017).

[22] Svetlana A. Zolotovskaya, Stefan Wackerow, Holger Neupert, Michael J. Barnes, Lorena Vega Cid, Benoit Teissandier, Ana Teresa Perez Fontenla, and Amin Abdolvand. High-performance thermal emitters based on laser-engineered metal surfaces. Optical Materials Express Vol. 10, Issue 2, pp. 622-631 (2020).

[23] W Huang, Y Li, R.E.N. Yanjie, J Sun, Z Xia, L Zhou, C Li, J Chen, Y Niu, Y Zhao. Effect of scanning speed on the high-temperature oxidation resistance and mechanical properties of Inconel 625 alloys fabricated by selective laser melting. Vacuum 206:111447 (2022).